Dissociation dynamics of the water dication following one-photon double ionization. II. Experiment

D. Reedy,[1,2] J. B. Williams,[1,*] B. Gaire,[3] A. Gatton,[3] M. Weller,[3] A. Menssen,[4] T. Bauer,[5] K. Henrichs,[5] Ph. Burzynski,[5] B. Berry,[6] Z. L. Streeter,[3,7] J. Sartor,[2] I. Ben-Itzhak,[6] T. Jahnke,[5] R. Dörner,[5] Th. Weber,[3] and A. L. Landers[2]

[1]*Department of Physics, University of Nevada, Reno, Reno, Nevada 89557, USA*

[2]*Department of Physics, Auburn University, Auburn, Alabama 36849, USA*

[3]*Lawrence Berkeley National Laboratory, Chemical Sciences and Ultrafast X-ray Science Laboratory, Berkeley, California 94720, USA*

[4]*Clarendon Laboratory, Department of Physics, University of Oxford, Oxford OX1 3PU, United Kingdom*

[5]*Institut für Kernphysik, J.W. Goethe Universität, Max-von-Laue-Str. 1, 60438 Frankfurt, Germany*

[6]*J. R. Macdonald Laboratory, Department of Physics, Kansas State University, Manhattan, Kansas 66506, USA*

[7]*Department of Applied Science, University of California, Davis, Davis, California 95616, USA*

(Received 27 April 2018; published 26 November 2018)

We demonstrate the use of cold target recoil ion momentum spectroscopy to perform state-selective measurements of the dissociative channels following single-photon double-ionization of H_2O. The two dominant dissociation channels observed lead to two-body ($OH^+ + H^+ + 2e^-$) and three-body ($2H^+ + O + 2e^-$) ionic fragmentation channels. In the two-body case we observe the presence of an autoionization process with a double-differential cross section that is similar to the single-photon double-ionization of helium well above threshold. In the three-body case, momentum and energy correlation maps in conjunction with new classical trajectory calculations in the companion theory paper by Z. L. Streeter *et al.* [Phys. Rev. A **98**, 053429 (2018)] lead to the determination of the eight populated dication states and their associated fragmentation geometry. For the latter case, state-specific relative cross sections, median kinetic energy releases, and median angles between asymptotic proton momenta are presented. This benchmark-level experiment demonstrates that, in principle, state-selective fixed-frame triple-differential cross sections can be measured for some dication states of the water molecule.

DOI: 10.1103/PhysRevA.98.053430

I. INTRODUCTION

Understanding the correlated emission of electron pairs from one-, two-, or multicenter Coulomb potentials after single-photon double-ionization (PDI) is a fundamental challenge both theoretically and experimentally [1–5]. There is an extensive literature on PDI for atomic targets, particularly helium, where the final state consists of three measurable continuum particles and the single initial state for the electron pair along with spherical symmetry allows for clear theoretical interpretation of experimental results [6–10]. Interpreting PDI spectra from molecules is substantially more challenging. While in atoms there is a distinct energy value above which the PDI can be initiated, this threshold is less clear for molecules. This is due to the additional degrees of freedom in the binding potential, which result in an entire threshold region [11]. At the upper limit of this threshold region is the direct, or vertical, ionization threshold wherein a single photon promotes a correlated electron pair to the continuum. Within the bounds of this threshold region indirect or two-step processes are possible, wherein the photon ejects one electron and leaves the cation in an excited state which, after rearrangement, can eject a second electron. In atoms, only discrete electronic states have to be taken into account, which in many cases can be clearly distinguished in the PDI measurement. However, the internuclear separation of the multicenter potential of a molecule results in a substantially more complex ground-state electronic configuration. Energy correlation maps, which depict the electron energy or electron energy sum as a function of the kinetic energy release (KER; sum of all neutral and ionic fragment kinetic energies), are one experimental tool that can probe the potential energy surfaces (PESs) and identify the electronic states involved in the dissociation; however, they are not always unambiguous, as some of the data below show.

Larger molecules such as triatomics can break up through multiple dissociation channels, further increasing the complexity of the PDI investigation. The relative populations of the final-state molecular fragments are governed by the often intricate dissociation channels on the PESs of the molecule. The binding energy of these surfaces varies as a function of the bending and (symmetric and asymmetric) stretching coordinates. Conical intersections and nonadiabatic transitions between the surfaces can allow energy distribution between the different modes and initiate nuclear rearrangements during the dissociation process of the molecular dication (e.g., vibration, rotation, isomerization [12], roaming [13]). Bond breakage can occur simultaneously or in a stepwise manner [14]. The number and kind of independent ways by which the dynamic nuclear system can move inherently increase the complexity of the correlated electron-pair emission process in their energy sharing and relative angles with respect to the body frame. It is therefore a challenge for theory

*jbwilliams@unr.edu

and experiment to identify and isolate all of these different contributions.

In PDI investigations of molecular targets, both experiment and theory heavily rely on simplifying assumptions such as the Born-Oppenheimer approximation [15] and the axial-recoil approximation [16]. The axial-recoil approximation, which assumes that constituent ion fragments proceed outward along bond axes following dissociation, paves the way to measure electron emission patterns in the body-fixed frame, if electrons can be detected in coincidence with the nuclear fragments [17–19]. Ideally, kinematically complete experiments can be performed, where the three-dimensional (3D) momenta of all particles are directly measured or derived for each PDI event. This enables the deduction of the kinetic energies and relative emission angles of all particles in the final state, generating highly (or even fully) differential cross sections.

Investigation of kinematically complete PDI of the simplest molecule, H_2, has been performed for more than a decade. Both theory [19–25] and experiment [3,18,26] have sought to probe the dynamics of electron correlation in the initial and final states.

Here we guide the reader through the detailed experimental exploration of the PDI of single water molecules, i.e., a simple planar triatomic target. The PDI experiment was performed with 57-eV photons, 18 eV above the vertical double-ionization threshold of 39 eV [27] for H_2O. In principle, the PDI of H_2O can lead to dissociation into the following two- and three-body breakup channels:

$$\gamma + H_2O \rightarrow H_2{}^{+*} + O^{+*} + 2e^- \quad (1)$$

$$\rightarrow H^+ + OH^{+*} + 2e^- \quad (2)$$

$$\rightarrow H^+ + H^* + O^{+*} + 2e^- \quad (3)$$

$$\rightarrow 2H^+ + O^* + 2e^- \quad (4)$$

$$\rightarrow O^{2+} + 2H^* + 2e^-, \quad (5)$$

where a superscript asterisk (*) indicates the possibility of either a ground or an excited state. Of these five channels only two have been observed in our PDI experiment, namely, one two-body, (2), and one three-body, (4), breakup. Channel (1) has been observed in proton-water collisions [28,29]. Experiments on PDI below the vertical ionization threshold of 39 eV have observed channel (3) [30], while electron ionization experiments have recorded fragments from all five channels [31]. In addition to PDI, single photoionization can produce an excited molecular fragment which later autoionizes, producing identical ion signatures as PDI processes [27]. We observed one such autoionization channel, namely,

$$\gamma + H_2O \rightarrow H^+ + OH^* + e^-, \quad (6)$$

where the OH^* molecule autoionizes to the OH^+ ion soon afterward.

The organization of the paper is as follows. In Sec. II we briefly discuss the setup used to produce the experimental data. In Sec. III we focus on the analysis of the observed two-body breakup. We present and discuss energy correlation maps, electron energy sharing results as single-differential cross sections (SDCSs), and relative electron-electron emission angles. The same spectroscopic analysis tools are applied to the observed three-body breakup in Sec. IV A. In Sec. IV B two new analysis diagrams are introduced: (a) the nuclear conformation map, i.e., the three-body yield as a function of the KER and the angle between asymptotic proton momenta (hereafter referred to as β), and (b) the triatomic breakup momentum plane. These new diagrams are introduced to identify and isolate, with the help of theory, all eight dication states relevant in this PDI experiment. We mention the unambiguous failure of the axial-recoil approximation, discovered and discussed in detail in the theoretical companion paper by Streeter *et al.* [32]. In Sec. V we conclude the investigation with a summary and outlook towards possible kinematically complete experiments on water molecules in the future.

II. EXPERIMENT

The current experiment was conducted using beamline 10.0.1 of the Advanced Light Source (ALS) at Lawrence Berkeley National Laboratory to produce 57-eV photons for the cold target recoil ion momentum spectroscopy (COLTRIMS) experimental chamber. A rigorous description of the COLTRIMS technique can be found in the literature [33–35]. In short, a supersonic molecular beam is crossed with a photon beam inside a spectrometer comprised of two microchannel plate, delay line anode detectors with static electric and magnetic fields used to steer the charged photo fragments onto the detectors. The expansion of the molecular beam through the nozzle and into vacuum leaves the molecules internally cold and overwhelmingly in their ground vibrational and rotational states. The ion detector had a two-layer anode, while the electron detector had a three-layer anode [36]. The molecular beam was produced by heating a liquid water reservoir and the input gas line to increase the vapor pressure of the water. A near-4π solid angle collection efficiency is realized for all charged particles, with detector dead-time issues preventing coincidence measurements of electrons striking the detector simultaneously in the same place. The detectors are position and time sensitive, allowing the full 3D momentum vectors for each charged particle to be calculated.

In the current case, up to two electrons are measured in coincidence with either a proton-OH^+ pair or two protons. Analysis was performed only on coincidence events including all four charged particles. For the latter measurement, a neutral (perhaps excited) oxygen atom is not measured. The large momentum difference between atomic and electronic fragments allows us to use conservation of linear momentum among atomic fragments to calculate the momentum of the neutral oxygen fragment. Broadening of momenta due to the laboratory-frame velocity of the gas jet was negligible. We include this calculated oxygen momentum in the analysis of the three-body breakup.

III. TWO-BODY BREAKUP

This section focuses on the dissociation dynamics of the two-body channel resulting in a proton and an OH^{+*} ion,

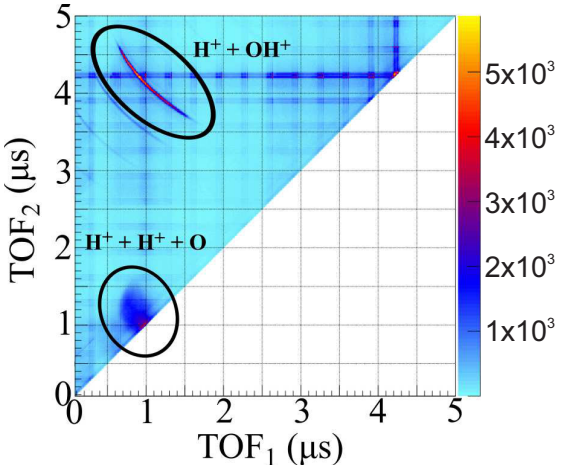

FIG. 1. Photoion-photoion coincidence spectrum, with the two-body and three-body channels circled. Coincidence yields are plotted as a function of the individual ion times of flight (TOF).

including the autoionizing channel. The channel is identified by its signature inthe photoion-photoion coincidence (PIPICO) spectrum (Fig. 1) as the narrow circled feature associated with H^+ and OH^+ ions measured in coincidence. Horizontal and vertical stripes crossing the spectrum are random coincidences corresponding to the 328.266-ns period at the ALS, while the circled round feature in the lower left corner identifies the three-body channel. Two "replicas" of the $H^+ + OH^+$ feature can be observed as well. These are identical in origin to the horizontal and vertical stripes: they are two-particle ion coincidences corresponding to the ALS bunch marker and erroneously paired with electron background signals by the acquisition system.

Once the channel is isolated in the PIPICO spectrum we proceed by considering the energy correlation map [Fig. 2(a)], which shows the $H^+ + OH^+$ yield as a function of the KER and electron energy sum ($E_{e\,\mathrm{sum}}$). A complementary correlation plot of the same yield as a function of the KER and individual electron energy is presented in Fig. 2(b). Both

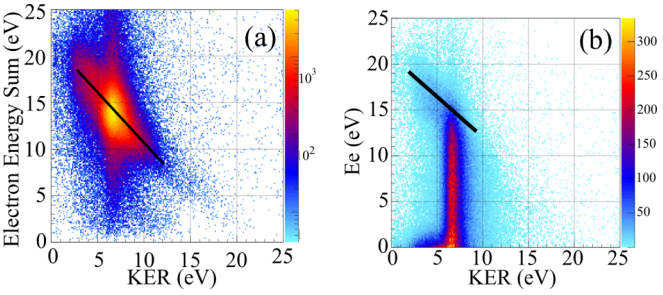

FIG. 2. (a) Energy correlation plot for the two-body breakup channel: $H^+ + OH^+$ yield as a function of the electron energy sum ($Ee_1 + Ee_2$) and KER (log-yield scaling). (b) Energy correlation plot for the two-body breakup channel: yield as a function of the single-electron energy and KER (lin-yield scaling). Both electrons are included in the plot. Black lines are added as a visual guide to the diagonal features.

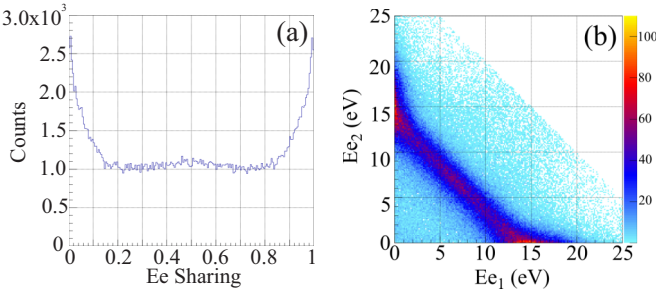

FIG. 3. (a) Electron yield of the $H^+ + OH^+$ channel as a function of the electron energy (E_e) sharing ratio, $E_{e\,1}/E_{e\,\mathrm{sum}}$. (b) Individual electron energies.

electrons from the coincidence measurement are included in the plot.

Gervais *et al.* [37] performed an exhaustive study of the eight lowest HDO^{2+} dication dissociation channels, four of which preferentially dissociate to the two-body channel. They found that these four dication states ($X\,^3A''$, $1\,^1A'$, $1\,^1A''$, and $2\,^1A'$ in C_S symmetry) dissociated with a KER near 7 eV. In this work we found a mean KER of 6.7 eV for the bright vertical feature in Figs. 2(a) and 2(b), which matches reasonably well the results in Ref. [37]. The width of the vertical feature in electron energy is due to the separation of the potential surfaces leading to the four states: the potential surface "shapes" are similar, leading to comparable KER values, but their relative heights above the H_2O ground state are different, leading to a broad range of electron energies. The extent of the vertical feature is exacerbated by the electron energy resolution.

Based solely on the analysis in Ref. [37], it is unclear what the diagonal feature observed in the energy correlation maps (Fig. 2) might represent. Instead, a study of two-step PDI of water by Sann *et al.* [27] using 43-eV photons provides evidence that this diagonal feature is a signature of an autoionization process. Single photoionization of the water molecule produces a proton and an excited OH fragment, which subsequently autoionizes to the $X\,^3\Sigma^-$ ground state of OH^+ once the proton is far enough away that the autoionization channel becomes energetically open. Measurement of the two ionic fragments, as well as the fast photoelectron and slow autoionization electron, is easily misinterpreted as a direct PDI event upon first inspection.

Comparing Fig. 1(b) in Ref. [27] to Fig. 2(b) here offers verification that we have observed the same autoionization process. The excess photon energy of the current experiment (57 eV instead of 43 eV), as well as the preponderance of direct PDI, manifest in the bright vertical stripe connecting the "fast electron" (diagonal feature) and "slow electron" (horizontal feature near 0). The electron energy sharing ratio is presented as a single differential cross section in Fig. 3(a). The electron energy correlation is presented in Fig. 3(b). Features along the axes in Fig. 3(b) correspond to the fast and slow electron energy pairs, while the diagonal feature corresponds to the symmetric electron energy sharing of a PDI process. In PDI of larger molecules, for example, in difluoroethylene $C_2H_2F_2$, the asymmetric energy sharing features appear below the diagonal, in contrast to the feature appearing above the

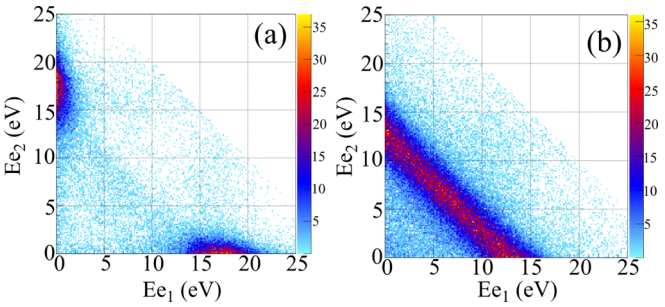

FIG. 4. Electron yield of the $H^+ + OH^+$ channel as a function of the individual electron energies with (a) KER < 5 eV, isolating the asymmetric energy sharing contribution, and (b) KER > 7 eV, isolating the symmetric energy sharing contribution.

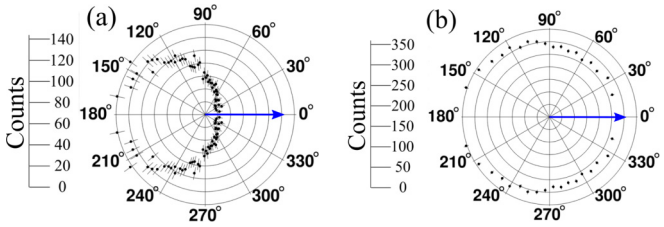

FIG. 5. Angle between the two emitted electrons. One electron is fixed at 0° (blue arrow). (a) A symmetric energy sharing electron pair, where each electron has $50\% \pm 5\% E_{\text{sum}}$, summed over all possible states. (b) An asymmetric energy sharing pair, where the fixed electron has $E_e > 90\% E_{\text{sum}}$, summed over all possible states. The distributions have been mirrored about a line between 0 and 180°.

diagonal in Fig. 3(b) [38]. This disparity is again likely resolved by consulting with Ref. [27]. The autoionizing channel leads to the OH^+ ground state $X^3\Sigma^-$, while PDI channels can lead to a number of excited cation states. Higher potential surfaces leave less energy to distribute among the photoelectrons in this case, which accordingly moves the diagonal feature in Fig. 3(b) toward the origin.

The two features in Fig. 3(b) can be separated to a large extent by requiring KER < 5 eV and KER > 7 eV, which elucidates the asymmetric and symmetric sharing features, respectively, as shown in Fig. 4. Separation of the asymmetric electron energy sharing via a gate on KER < 5 eV is consistent with techniques used in Ref. [27] which separated the autoionization channel with similar "low-KER" gating.

We note that in Ref. [27], significantly less direct PDI was observed than in the current data. This is due to the lower photon energy of 43 eV being closer to the direct PDI threshold. Among the PDI events observed, there is a preference for equal electron energy sharing, which can be best observed in the small bright spot in the center of the diagonal feature in Fig. 3(b). This tendency toward equal energy sharing in the PDI case is discussed in detail in Sec. IV for the three-body case.

Eland *et al.* [39] and others have observed indirect dissociative double-ionization processes below the vertical double-ionization threshold, as low as 34 eV photon energy. The signature of such an autoionization event is one electron with nearly all the excess photon energy paired with an electron of near-zero energy. In the current experiment, a 57-eV photon would impart ~23 eV to the photoelectron in such a process. The current data do not display any significant signature corresponding to such a dissociation pathway.

Further separation of the PDI data in the two-body channel is extremely challenging due to the lack of separable features. Gervais *et al.* [37], and more recently Ref. [32], inform us that the PDI data are likely a combination of primarily the $^3A_2$, $1\ ^1A_1$, $^1A_2$, and $2\ ^1A_1$ dication states. However, these states cannot be separated in the current data set.

Despite the difficulty in identifying individual dication states in the two-body channel, we are able to report two sets of doubly differential cross sections. The first is the relative electron-electron emission angle for both symmetric and highly asymmetric electron energy sharings (SDCS values of near 0.5 ± 0.1 and near 0 ± 0.1), shown in Fig. 5. The second is the electron emission angle relative to the polarization axis for asymmetric energy sharing pairs, shown in Fig. 6. For the PDI process, i.e., the symmetric energy sharing case, the cross sections are integrated over all possible dication states.

Figures 5(a) and 5(b) show the relative electron-electron emission angular distributions for symmetric and asymmetric energy sharings, respectively. The distribution for symmetric energy sharing [Fig. 5(a)] resembles the predictions of atomic "knockoff" (or "knockout") models for angular distributions following double-photoionization well above threshold [40]. In this case, one expects symmetric energy sharing and a billiard-ball 90° angular peak, which skews toward 180° due to Coulomb repulsion. Figure 5(a) represents the PDI case, where the photon promotes two correlated electrons to the continuum and a dication state is populated directly. The completeness of this particular measurement is, however, limited by the electron detector dead time, particularly where equal-energy electrons with nearly identical momentum vectors can hit the detector at the same place and time, causing the loss of the multihit event. We present the measurement here with the caveat that although general trends in this distribution are likely correct, the measurement should be confirmed in a future experiment with reduced phase-space lapse, leading to multihit event losses.

The distribution of the angle between the photoelectrons in the case of highly asymmetric energy sharing, i.e., the autoionization case, is shown in Fig. 5(b). This distribution

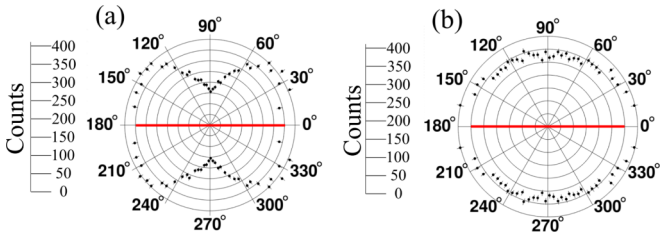

FIG. 6. Laboratory-frame angular distributions of asymmetric energy sharing electron pairs for the two-body breakup. The polarization axis of the incident photon is indicated by the red line. (a) Fast electron with $E_e > 0.9 E_{\text{sum}}$. (b) Slow electron with $E_e < 0.1 E_{\text{sum}}$. The distributions have been symmetrized over the 0–180° axis.

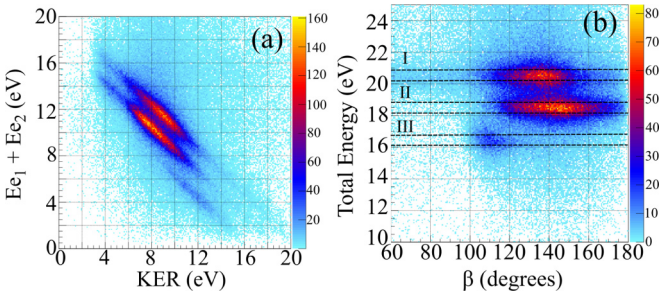

FIG. 7. Energy correlation plots for the three-body breakup, including investigation of the angle between proton momenta. (a) $H^+ + H^+ + O$ yield as a function of the electron energy sum ($E_{e\,\mathrm{sum}}$) and KER. (b) Yield as a function of the total energy ($E_{e\,\mathrm{sum}}$ + KER) and β (asymptotic angle between proton momenta). The three labeled features correspond to asymptotic oxygen terms: I, ^3P; II, ^1D; III, ^1S.

meets expectations for an autoionization process, where the slow electron has no "knowledge" of the fast electron's momenta and is emitted isotropically in a second step.

Figures 6(a) and 6(b) show the laboratory-frame photoelectron angular distributions with respect to the photon polarization axis. Figure 6(a) is the distribution of the fast electron of an asymmetric energy sharing pair, carrying >90% of the total electron energy. Figure 6(b) is the distribution of a slow electron in an asymmetric pair, carrying <10% of the total electron energy. Figures 6(a) and 6(b) resemble the distributions presented by Knapp *et al.* [41] and Colgan *et al.* [20] following double-photoionization of helium well above threshold. Both studies found that the fast electron had a pronounced dip around 90°, similar to a dipole transition to the continuum. The similarity of their finding to those in Fig. 6(a) suggests that the fast photoelectron measured here is emitted from an orbital of mainly atomic S character. In addition, they found that the slow electron had an essentially isotropic distribution, which was also the finding in Fig. 6(b).

IV. THREE-BODY BREAKUP

We begin the analysis by repeating the approach employed in the two-body case with energy correlation maps, electron energy sharing, and angular analysis, described in Sec. IV A. Successful identification of features in the energy correlation map leads us in a new direction, which is described in Sec. IV B.

A. Energy correlation maps, electron energy sharing, and electron emission angles

Analysis of the three-body reaction channel begins with identification of the channel in the PIPICO spectrum as the broad, round feature near the origin. The next steps follow the path of the two-body channel analysis, with continuum energy correlation maps. Since the three-body breakup has an angular component among the ionic fragments, an additional spectrum is presented in Fig. 7(b), namely, the $H^+ + H^+ + O^*$ yield as a function of the total continuum energy (sum of KER and electron energies) and β.

TABLE I. Oxygen term energy separation.

Term	NIST (eV)	Expt (eV)	Label
^3P	0.0	0.0	I
^1D	1.967	1.94 ± 0.51	II
^1S	4.190	4.02 ± 0.63	III

In contrast with the two-body case, there are separated features in the energy correlation map shown in Fig. 7(a). Three features of the distinct total continuum energy are visible. These features correspond to the lowest three energy terms of the neutral oxygen fragment, ^3P, ^1D, and ^1S, the asymptotic limits of the dissociating dication potential energy surfaces leading to $H^+ + H^+ + O$ and discussed in great detail by Gervais *et al.* [37] and in Ref. [32]. These features are labeled in Fig. 7(b), and their energies are shown in Table I along with NIST data of Moore [42]. The features labeled I, II, and III correspond to the $O(^3P)$, $O(^1D)$, and $O(^1S)$ asymptotes, respectively.

The electron energy sharing SDCS for the three-body breakup in Fig. 8(a) displays a structure different from that of the two-body breakup shown in Fig. 3(a). The distribution peaks at the center, indicating a strong preference for a near-symmetric energy sharing between the photoelectrons. In contrast with the two-body breakup, the data do not reveal a different energy sharing between the photoelectrons. While autoionization to $H^+ + O^+ + H$ is energetically possible, such a breakup was not observed in these data.

We attribute the center-peaked feature of the three-body PDI channel to a reduction of the electron energy phase space due to the relatively low photon energy. The binding energy of the electrons (39 eV) is higher than the excess energy of the photoelectrons (<18 eV). The competing process to direct PDI is the recapture of one electron; near threshold, if the photoelectrons do not share energy nearly evenly, the slow electron can be recaptured, resulting in a single-ionization or multistep autoionization process rather than direct PDI. The shape of the SDCS in this case is determined by the Wannier threshold geometry and energetic phase-space volume [43–46]. As recapture is more likely for asymmetric electron energy sharings, symmetric sharings are measured more often and the resulting SDCS resembles the center-peaked feature shown in Fig. 8(a). Accordingly, Fig. 8(b) shows no bright

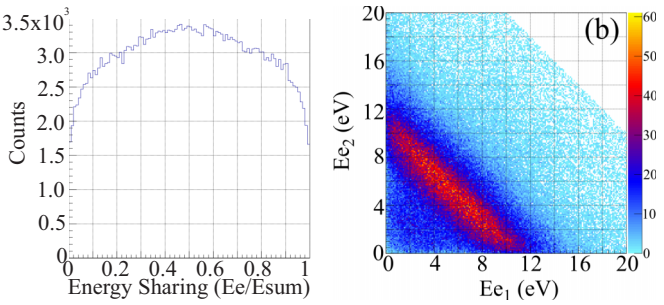

FIG. 8. $H^+ + H^+ + O$ yield as a function of (a) the electron energy (E_e) sharing ratio, $E_{e\,1}/E_{e\,\mathrm{sum}}$, and (b) the individual electron energies.

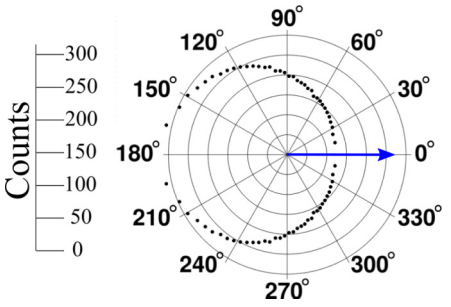

FIG. 9. Angle between the two emitted electrons. One electron is fixed at 0° (blue arrow). Data are summed over all electron energy sharings, all molecular orientations, and all possible dication states. The distribution has been mirrored about a line between 0 and 180°.

features along the ordinate and abscissa and only a diagonal feature which corresponds to symmetric energy sharing.

Figure 9 presents the angle between the momenta of the two electrons. This figure is similar to the findings from the two-body channel in the case where the electrons have nearly equal energy, i.e., the direct PDI case. As in the two-body case, this distribution is presented with the caveat that the angular distribution is limited by electron detector dead time and the measurement should be confirmed in future experiments with an emphasis on improved resolution for equal energy sharing electron pairs.

B. Nuclear conformation maps and molecular momentum planes

It is well known that the two hydrogen nuclei bind to the central oxygen atom via covalent bonding in the H_2O electronic ground state. Interactions between the binding electrons and the nuclear charges perturb the geometry of the molecule such that the minima of the bending potential occur at ∼104.5°. While the two-body channel offers no information regarding the bond angle at the time of photoionization, detection of the 3D momenta of the outgoing protons in coincidence allows us to infer the momentum of the oxygen atom via linear momentum conservation as described in Sec. I. This enables us to determine the asymptotic angle between proton momenta, β. It is clear in Fig. 7(b) that the asymptotic

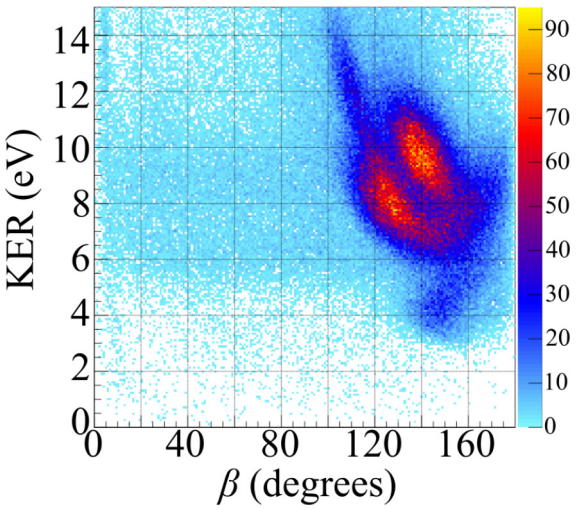

FIG. 10. $H^+ + H^+ + O$ yield as a function of the KER and β; dubbed nuclear conformation map.

limits of the dissociating dications leading to $O(^3P)$, $O(^1D)$, and $O(^1S)$ have unique β distributions.

As the water dication populates various PESs, we should expect changes in bond angle and OH bond lengths as the dication is rearranged according to the new dication molecular potential. Changes in the bond angle and bond lengths can manifest in both KER and β. To investigate these possibilities, we visualize the yield of the three-body channel as a function of the KER and β, shown in Fig. 10. Hereafter, such figures are referred to as nuclear conformation maps. Yield plots contrasting various dissociation angles and energies have been used in the literature to, for example, distinguish between concerted and stepwise bond cleavage in molecular systems [14].

Knowledge of the water dication potential surfaces and their asymptotes from Ref. [32] leads us to conclude that the features in Fig. 10 must correspond to the various dication states populated by the PDI. As each dication state dissociates to a particular total continuum energy asymptote, easily identified by the neutral oxygen term, we can produce nuclear conformation maps using the total continuum energy gates shown in Fig. 7(b). The conformation maps produced with

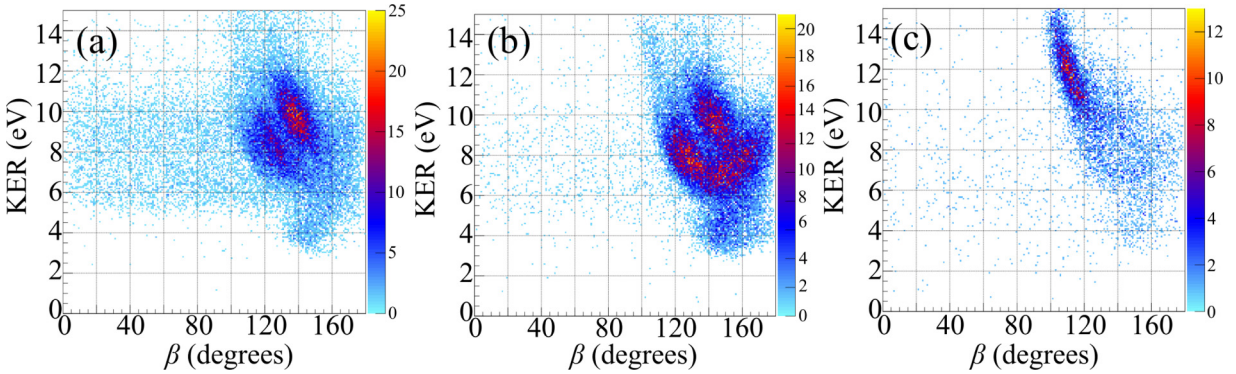

FIG. 11. Nuclear conformation maps, restricted by the total continuum energy as shown in Fig. 7(b). (a) Gate I, corresponding to the $O(^3P)$ asymptote. (b) Gate II, corresponding to the $O(^1D)$ asymptote. (c) Gate III, corresponding to the $O(^1S)$ asymptote.

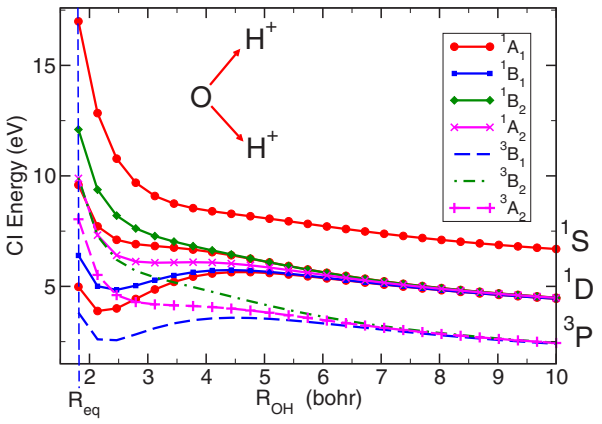

FIG. 12. Slice of the nine energetically accessible dication potential curves along a bond angle of 104.5° and under symmetric stretch ($R_1 = R_2$). The nearness of the dication curves at R_{eq} suggests the origin of the overlap of the states in the nuclear conformation map.

these total continuum energy gates will then be limited to the dication states that dissociate to the corresponding oxygen asymptote. The results of these total continuum energy gates on the nuclear conformation map are shown in Fig. 11.

Before further discussion of the features in Fig. 11, it is highly informative to pause and take further guidance from the theory provided in Ref. [32], as the computed potential surfaces suggest that each oxygen asymptote is associated with specific dication states: The triplet dication states $^3B_1$, $^3A_2$, and $^3B_2$ lead to the O(^3P) asymptote; the singlet dication states $1\,^1A_1$, $2\,^1A_1$, $^1A_2$, $^1B_1$, and $^1B_2$ lead to the O(^1D) asymptote; and the one-singlet dication state, $3\,^1A_1$, leads to the O(^1S) asymptote. The asymptotic behavior of these dication states is shown in Fig. 12. Branching ratios presented in Ref. [32] and Ref. [37] suggest that the $1\,^1A_1$ dication dissociates nearly exclusively to the two-body channel $H^+ + OH^+$. Consequently, for a three-body dissociation, we expect three dication states to lead to the O(^3P) asymptote, four to the O(^1D), and one to the O(^1S).

The nuclear conformation maps in Fig. 11, gated on the total continuum energy corresponding to each final oxygen term, match results in Fig. 9 in Ref. [32], wherein classical trajectory simulations were used to produce nuclear conformation maps for each of the eight anticipated dication states. These simulations were grouped by the dication states that have identical asymptotic continuum energies, i.e., by the oxygen term. In the simulations, each dication state appears to have a characteristic combination of KER and angle β.

It is now apparent that the combination of asymptotic continuum energy (corresponding to the neutral oxygen term), KER, and β might be used as a signature to select individual dication states in the data as they dissociate into the three-body channel $H^+ + H^+ + O^*$. The results from Ref. [32] show that there is some significant overlap in these states, particularly those leading to the O(^1D) asymptote. The nearness of the $^1B_2$, $2\,^1A_1$, and $^1A_2$ potential surface slices, shown in Fig. 12, helps visualize this overlap.

We use the prescribed combination of asymptotic continuum energy, KER, and β from Ref. [32] to create state-selection gates for each of the eight dication states of the dissociating water molecule. The gates are polygons surrounding each dication state in the conformation map. The polygon gates are summarized in Table II and visualized in Fig. 13.

TABLE II. Gates used to state-select three-body breakup on conformation maps.

C_{2v}	Points (β,KER)
$^3B_1$	(130,2.5),(130,4.6),(175,4.6),(175,2.5)
$^3A_2$	(105,11),(107,11),(147,6.5),(147,5.2),(105,5.2)
$^3B_2$	(115,12),(165,12),(165,6.4),(150,6.4),(115,10.3)
$^1B_1$	(130,4.6),(175,4.6),(175,2.5),(130,2.5)
$^1A_2$	(105,11),(107,11),(135,7.3),(135,5.5),(105,5.5)
$2\,^1A_1$	(150,6),(151,7.8),(180,12),(180,6)
$^1B_2$	(115,12),(160,12),(160,9.4),(147,7),(115,10.5)
$3\,^1A_1$	(90,7),(90,18),(145,18),(145,7)

For the given data set, we chose gates both to minimize cross-state contamination and to maximize total events. The application of these gates excludes some valid data from each state, while admitting some contamination from nearby states in the conformation map space. We apply the gates to classical trajectory calculations from Ref. [32] to characterize the quality of the state selection in two ways. First, we observe the distribution of the different states present in the gated data, i.e., the state prevalence. Second, we observe the amount of the selected state present in the gate as a fraction of the total number of simulated events for that state, i.e., the state fraction. Table III shows the state prevalence and state fraction for each selected state. The left column lists the selected state's C_{2v} symbol. The right column lists the state fractions. The central columns indicate the prevalence of each state.

With the gates from Table II, the states are selected with better than 91% targeted state prevalence for all states except $2\,^1A_1$. We anticipate that with a more robust data set and more refined gates, many of these values can be improved. From visual inspection of Figs. 13 and 9 in Ref. [32] it is clear that we lose a significant number of events from all dication states leading to the O(^1D) asymptote due to their overlap in the conformation map around KER = 6 eV and $\beta = 140°$.

Using the state-selection gates listed in Table II, we list the relative cross sections for the states as approximate percentages of all three-body data in Table IV. These relative cross sections are produced by applying the state-selection gates for

TABLE III. Dication prevalence and fraction by state-selection gate (%).

Selected	State prevalence (%)								Fraction
state	$^3B_1$	$^3A_2$	$^3B_2$	$^1B_1$	$^1A_2$	$2\,^1A_1$	$^1B_2$	$3\,^1A_1$	(%)
$^3B_1$	96.7	3.3	0	—	—	—	—	—	67.8
$^3A_2$	0.4	98.3	1.3	—	—	—	—	—	84.8
$^3B_2$	0	4.7	95.3	—	—	—	—	—	93.6
$^1B_1$	—	—	—	94.0	6.0	0	0	—	59.5
$^1A_2$	—	—	—	0	91.2	8.0	0.8	—	77.5
$2\,^1A_1$	—	—	—	2.5	3.9	83.8	9.8	—	53.1
$^1B_2$	—	—	—	0	2.4	3.9	93.7	—	81.9
$3\,^1A_1$	—	—	—	—	—	—	—	100	100

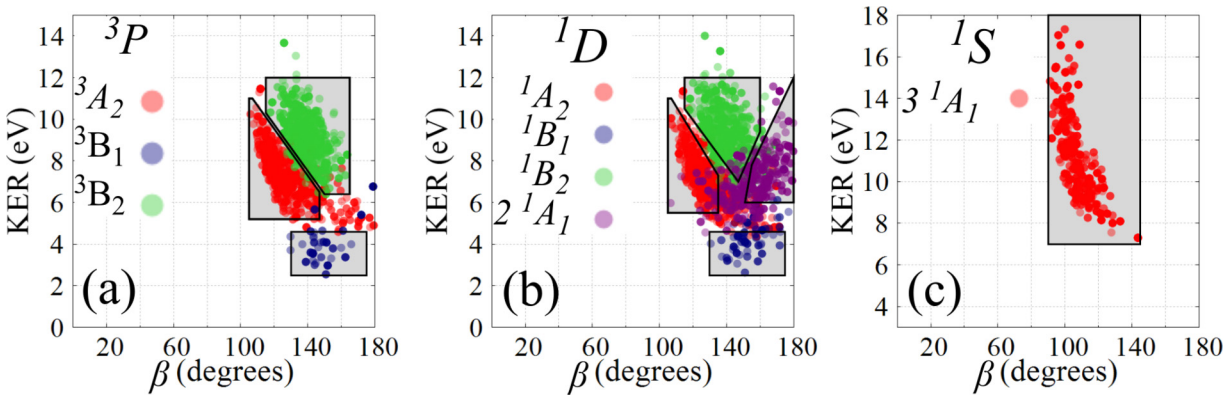

FIG. 13. Gates are constructed as polygons of connected points surrounding each dication state in conformation map space. Table II lists the points used to construct each polygon.

each of the eight dication states and reporting the fractional yield of the coincidence measurement.

In addition to the relative cross sections, we report the peak values for the KER and β for each dication state, listed in Table V. The standard deviation for each gated distribution is reported along with the peak value.

It bears repeating that in Tables IV and V, the quality of the state-specific separations of the data varies. We have quantified the severity of cross-state contamination in Table III. Despite this caveat, the agreement with results in Ref. [32] for KER and β values is encouraging.

In addition to the KER, β, and fractional yield measurements, knowledge of the 3D momentum vectors of each molecular fragment gives us access to another powerful analysis tool. The momenta of the particles can be visualized in the molecular momentum plane defined by the proton momenta. Specifically, we define the z axis for the molecular plane as

$$\frac{\hat{p}_1 + \hat{p}_2}{|\hat{p}_1 + \hat{p}_2|} = \hat{z}_{\text{mol}}. \tag{7}$$

The y axis is defined as the perpendicular coplanar axis, as shown in the center of Fig. 15. This allows us to form a Newton-like plot of the fragments in the molecular dissociation plane. Under the axial-recoil approximation, such plots would reveal the dynamics of the dissociating water dication in the rest frame of the molecule. However, results in Ref. [32] suggest that the axial-recoil approximation fails, in some cases dramatically, for the PDI of water. As a result, the Newton-like plots serve as a visual guide to the asymptotic dissociation and a probe for theoretical results without reliance on the axial-recoil approximation. The current experiment and analysis produce asymptotic momenta for each particle, and as a result, the experiment itself is unable to determine whether or not the axial-recoil approximation has failed without input from theory.

The Newton-like momentum plot, integrated over all dication states, is presented in Fig. 14. From previous analysis of the conformation maps in this paper we expect that this Newton-like plot should have distinct values of momenta and β for each dication state. Separation of the individual dication states in the Newton-like plot is achieved by the application of the state-selection gates reported in Table II. These state-selected Newton-like plots are presented in Fig. 15.

Using all the tools developed in Sec. IV B and guidance from Ref. [32], Fig. 15 provides dissociation frame momentum plots which separate each of the eight dication states. These figures are produced by limiting the total continuum asymptotic energy as in Fig. 7(b) and by limiting the KER and β according to the unique features of the nuclear conformation maps identified using the classical trajectory simulations from Ref. [32]. The details of these gates are reported in Table II and Fig. 13. The assignment of particular dication state labels follows guidance from Ref. [32].

Simulation results from Ref. [32] were used to reproduce the Newton-like figures, shown in Fig. 16. These figures

TABLE IV. Approximate state-specific relative cross sections for the three-body breakup.

C_{2v} symmetry	% of 3-body data ($\sqrt{N}$)
$1\,^1A_1$	—
$^3B_1$	1.45 (0.05)
$^3A_2$	12.75 (0.15)
$^3B_2$	25.28 (0.21)
$^1B_1$	2.93 (0.07)
$^1A_2$	13.77 (0.15)
$2\,^1A_1$	13.24 (0.15)
$^1B_2$	20.87 (0.19)
$3\,^1A_1$	9.71 (0.13)

TABLE V. Peak KERs and βs from experimental data (expt.) and simulations [32] for the three-body breakup.

C_{2v}	Expt. KER (σ)	KER	Expt. β (σ)	β
$^3B_1$	4.29 (0.42)	4.2	145.9 (8.7)	152.2
$^3A_2$	7.99 (1.14)	7.3	121.4 (9.8)	129.0
$^3B_2$	9.66 (1.22)	9.2	138.6 (10.7)	138.5
$^1B_1$	4.26 (0.41)	4.2	148.3 (10.1)	154.9
$^1A_2$	7.58 (0.98)	7.2	125.5 (8.0)	130.0
$2\,^1A_1$	7.65 (1.03)	7.1	163.6 (6.7)	155.8
$^1B_2$	9.81 (1.11)	9.3	142.9 (9.3)	140.5
$3\,^1A_1$	11.4 (1.83)	11.4	110.8 (11.4)	106.0

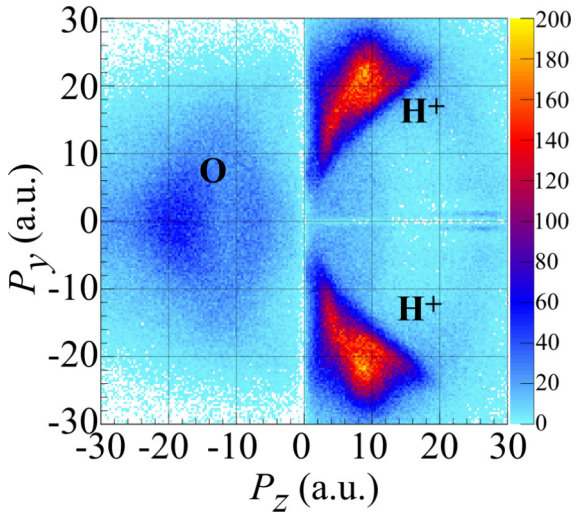

FIG. 14. Newton-like plot of the dissociating water molecule, in the molecular dissociation frame, for the three-body breakup. The horizontal axis is along the sum of the proton unit momenta. Protons are in the first or second quadrant, by definition, while the oxygen momentum is in the third and fourth quadrants.

provide further evidence that the state-selection gates in Table II are separating the correct dication states. The axial-recoil approximation was not needed to make this comparison, as Ref. [32] reproduced the results of the direct physical observable, e.g., the asymptotic momenta.

V. CONCLUSIONS

We have measured the 3D momenta of two ionic fragments and two electrons in coincidence following the PDI of water molecules with single linearly polarized photons of 57 eV. The analysis was split to focus separately on (a) the observed two-body reaction channel, $H^+ + OH^+$, and (b) the three-body channel, $H^+ + H^+ + O^*$.

(a) Energy correlation maps (Fig. 2), single-differential cross sections (Fig. 3), double-differential cross sections of electron-electron emission angles and electron angular distributions with respect to the polarization axis (Figs. 5 and 6) revealed a rich body of data due to at least four dication states and OH^+ fragment vibronic and rotational excitation. Furthermore, it was found that the PDI channel was overlayed with an autoionization process. Unique single-differential cross-section distributions were observed for states dissociating via

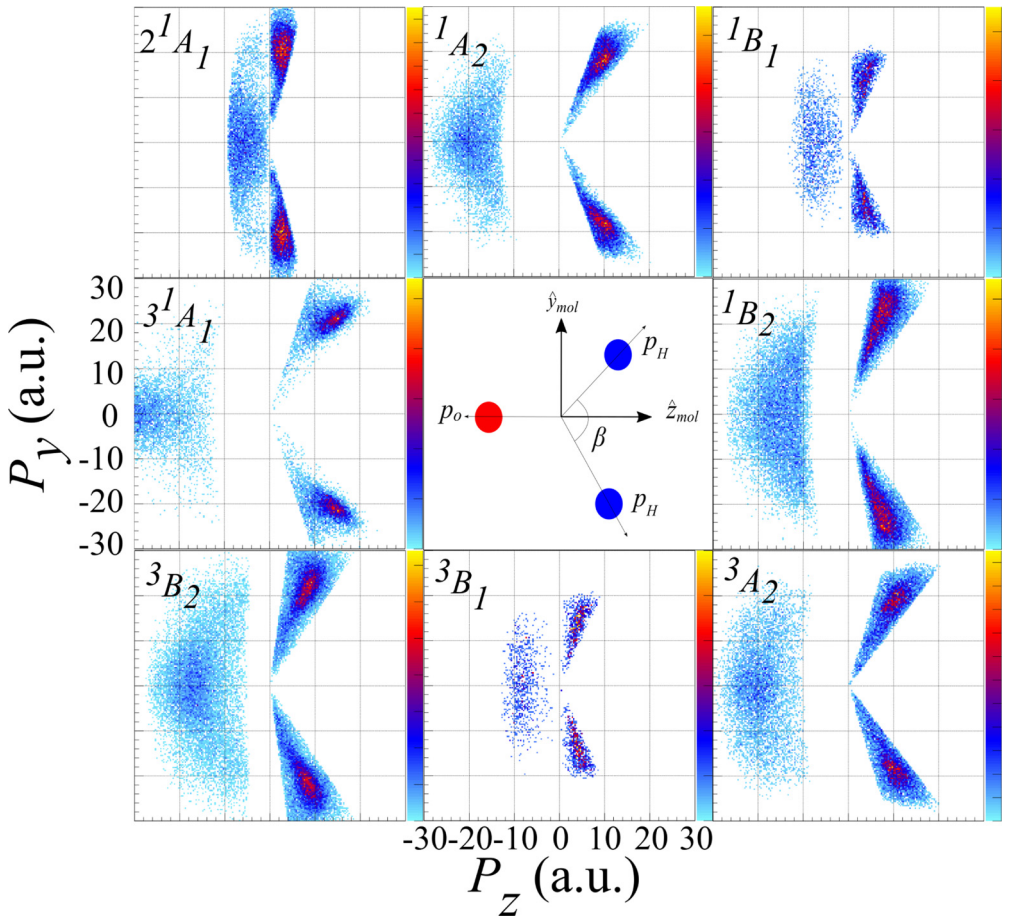

FIG. 15. Momentum plots as in Fig. 14, with the gates of the total energy [Fig. 7(b)] and the KER and β listed in Table II applied to separate the individual dication states. The selected state of each panel is noted in the upper left corner. The schematic in the center panel reminds the reader about the dissociation frame axes and the positions of the oxygen (red circle) and protons (blue circles). Axis scales are identical in each panel but are provided only once to improve the visual clarity.

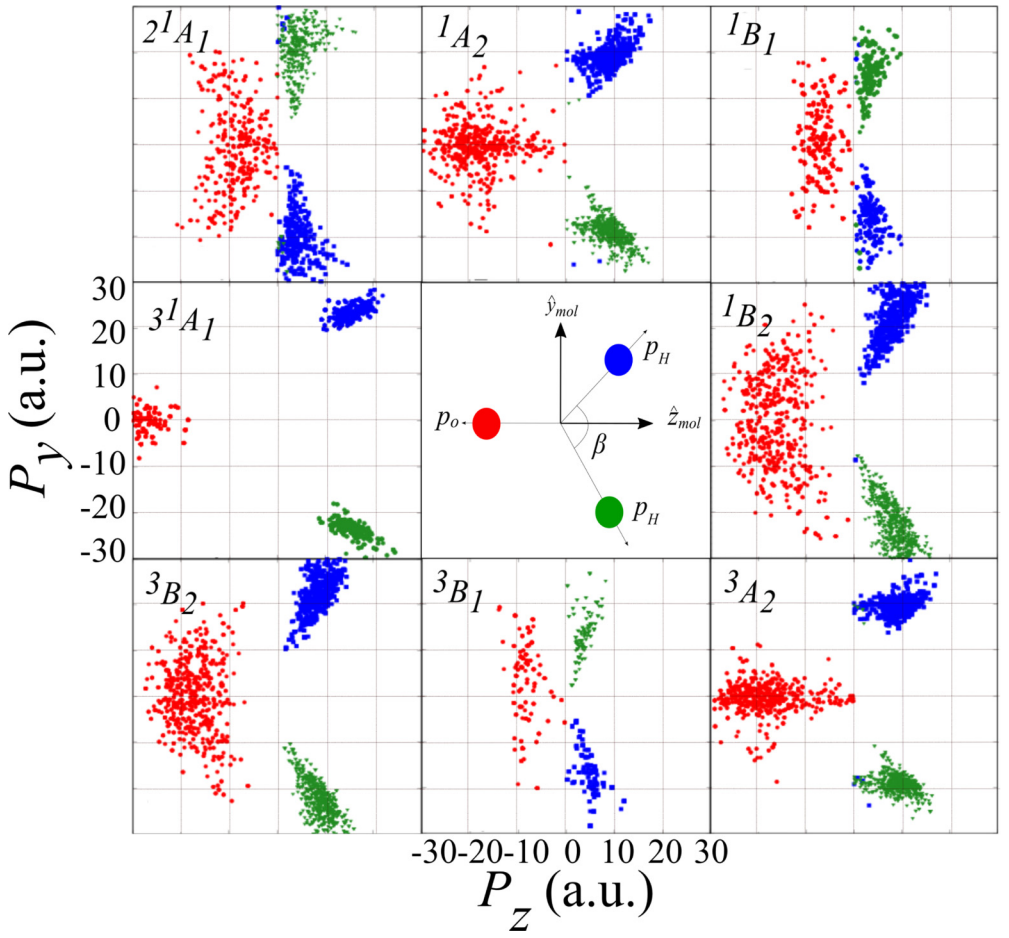

FIG. 16. Momentum plots as in Fig. 14 for all eight dication states using classical trajectory simulation results from Ref. [32] for the three-body breakup and in the experimental dissociation frame. The state of each panel is noted in the upper left corner. The schematic in the center panel reminds the reader about the experimental dissociation frame axes and the positions of the oxygen (red circle) and protons (blue and green circles). Axis scales are identical in each panel but are provided only once to improve the visual clarity.

autoionization and those dissociating via direct PDI. Identification of dication states $X\,^3A''$, $1\,^1A'$, $1\,^1A''$, and $2\,^1A'$ could not be realized without more separable data or guidance from theory. Since measurements of the final-state dissociation angles are not a measurable quantity in the two-body breakup, only a highly resolved measurement of the energy correlation map (Fig. 2) might offer access to these states. This would require a larger data set than was realized in this experiment.

(b) Spectra similar to those in paragraph (a) were used to investigate the dissociation dynamics, as well as a new nuclear conformation map (Fig. 10) and Newton-like plots (Fig. 14). Analysis of the electron single- and double-differential cross sections (Figs. 8 and 9) were similar to those of the two-body channel for equal energy sharing but showed no signs of extreme electron energy asymmetry following indirect autoionization channels. Nuclear conformation maps and guidance from Ref. [32] provided a way to state-select the three-body fragmentation. The most contaminated data following state selection was the $2\,^1A_1$ state, which included no more than ~83% of the selected state following the application of the gate. In contrast, the other seven gates provided better than ~91% state prevalence in each case. With the state-selection gates, we extracted state-specific peak kinetic energy releases (KERs) and βs and compared them to the results from classical trajectory simulations in Ref. [32]. Furthermore, we have presented the first experimental relative cross sections for these eight dication states following further guidance from Ref. [32].

In principle, the experimental selection and molecular plane orientation of the dication states can be used to make state-selected, fixed dissociation-frame triply differential cross-section (TDCS) measurements. Results from Ref. [32] suggest that three states, namely, $2\,^1A_1$, $^1B_1$, and $^3B_1$, cannot be described as adhering to the axial-recoil approximation in any way. The rest of the states can be state selected and body frame oriented. From the gates presented in Sec. IV B, we can determine state-selected and body-frame-oriented TDCSs. These cross sections, typically presented as an angle between photoelectrons with the energy sharing ratio and body frame fixed, are exquisitely sensitive to electron-electron correlation as determined by the initial two-electron wave function, selection rules based on parity and angular momentum conservation depending on the energy sharing of the two electrons, symmetry effects of the populated molecular dication state, and Coulomb interactions of all free charged particles. While the measurement of TDCSs has been

nicely realized in great detail for the PDI of H_2 (resp. D_2) [3,18,19,25,26], such investigations already become demanding for the PDI of diatomics like N_2 and O_2 due to the multitude of electronic states involved in the near-threshold region. Few successful experiments have been performed on these diatomic systems [47,48]. Advancing towards such highly detailed PDI studies of small polyatomics represents a challenge for theory and experiment alike. The new spectroscopic analysis tools presented here will be used to produce clean and powerful TDCS measurements in future investigations.

ACKNOWLEDGMENTS

Work performed at University of Nevada, Reno, was supported by University of Nevada, Reno, and National Science Foundation Grant No. NSF-PHY-1807017. Work at LBNL was performed under the auspices of the U.S. Department of Energy (DOE) under Contract No. DEAC02-05CH11231, using the Advanced Light Source (ALS) and National Energy Research Computing Center (NERSC), and was supported by the ALS, U.S. DOE, Office of Basic Energy Sciences, Division of Chemical Sciences. We thank the staff of the ALS, in particular, beamline 10.0.1 scientists, for their outstanding support. JRML personnel were supported by Grant No. DE-FG02-86ER13491 from the same funding agency. A.S.G. acknowledges financial support from the ALS via the Doctoral Fellowship in Residence. Our collaborators from Goethe University Frankfurt acknowledge support by DAAD and BMBF. We are indebted to the RoentDek Company for long-term support with detector hardware and software.

[1] A. S. Kheifets, Phys. Rev. A **71**, 022704 (2005).
[2] L. Malegat, P. Selles, and A. Huetz, J. Phys. B **30**, 251 (1997).
[3] M. Waitz, D. Metz, J. Lower, C. Schober, M. Keiling, M. Pitzer, K. Mertens, M. Martins, J. Viefhaus, S. Klumpp, T. Weber, H. Schmidt-Böcking, L. P. H. Schmidt, F. Morales, S. Miyabe, T. N. Rescigno, C. W. McCurdy, F. Martín, J. B. Williams, M. S. Schöffler, T. Jahnke, and R. Dörner, Phys. Rev. Lett. **117**, 083002 (2016).
[4] D. Akoury, K. Kreidi, T. Jahnke, T. Weber, A. Staudte, M. Schöffler, N. Neumann, J. Titze, L. P. H. Schmidt, A. Czasch, O. Jagutzki, R. A. C. Fraga, R. E. Grisenti, R. D. Muiño, N. A. Cherepkov, S. K. Semenov, P. Ranitovic, C. L. Cocke, T. Osipov, H. Adaniya, J. C. Thompson, M. H. Prior, A. Belkacem, A. L. Landers, H. Schmidt-Böcking, and R. Dörner, Science **318**, 949 (2007).
[5] L. Cederbaum, F. Tarantelli, A. Sgamellotti, and J. Schirmer, J. Chem. Phys. **85**, 6513 (1986).
[6] R. Dörner, H. Bräuning, J. M. Feagin, V. Mergel, O. Jagutzki, L. Spielberger, T. Vogt, H. Khemliche, M. H. Prior, J. Ullrich, C. L. Cocke, and H. Schmidt-Böcking, Phys. Rev. A **57**, 1074 (1998).
[7] H. Bräuning, R. Dörner, C. L. Cocke, M. H. Prior, B. Krässig, A. Bräuning-Demian, K. Carnes, S. Dreuil, V. Mergel, P. Richard, J. Ullrich, and H. Schmidt-Böcking, J. Phys. B **30**, L649 (1997).
[8] P. Bolognesi, R. Camilloni, M. Coreno, G. Turri, J. Berakdar, A. S. Kheifets, and L. Avaldi, J. Phys. B **34**, 3193 (2001).
[9] J. S. Briggs and V. Schmidt, J. Phys. B **33**, R1 (2000).
[10] H. Bräuning, R. Dörner, C. L. Cocke, M. H. Prior, B. Krässig, A. S. Kheifets, I. Bray, A. Bräuning-Demian, K. Carnes, S. Dreuil, V. Mergel, P. Richard, J. Ullrich, and H. Schmidt-Böcking, J. Phys. B **31**, 5149 (1998).
[11] D. Winkoun, G. Dujardin, L. Hellner, and M. J. Besnard, J. Phys. B **21**, 1385 (1988).
[12] Y. H. Jiang, A. Rudenko, O. Herrwerth, L. Foucar, M. Kurka, K. U. Kühnel, M. Lezius, M. F. Kling, J. van Tilborg, A. Belkacem, K. Ueda, S. Düsterer, R. Treusch, C. D. Schröter, R. Moshammer, and J. Ullrich, Phys. Rev. Lett. **105**, 263002 (2010).
[13] A. G. Suits, Acc. Chem. Res. **41**, 873 (2008).
[14] J. Rajput, T. Severt, B. Berry, B. Jochim, P. Feizollah, B. Kaderiya, M. Zohrabi, U. Ablikim, F. Ziaee, K. Raju P., D. Rolles, A. Rudenko, K. D. Carnes, B. D. Esry, and I. Ben-Itzhak, Phys. Rev. Lett. **120**, 103001 (2018).
[15] A. Tachibana and T. Iwai, Phys. Rev. A **33**, 2262 (1986).
[16] R. M. Wood, Q. Zheng, A. K. Edwards, and M. A. Mangan, Rev. Sci. Instrum. **68**, 1382 (1997).
[17] A. Landers, T. Weber, I. Ali, A. Cassimi, M. Hattass, O. Jagutzki, A. Nauert, T. Osipov, A. Staudte, M. H. Prior, H. Schmidt-Böcking, C. L. Cocke, and R. Dörner, Phys. Rev. Lett. **87**, 013002 (2001).
[18] T. Weber, A. Czasch, O. Jagutzki, A. Müller, V. Mergel, A. Kheifets, J. Feagin, E. Rotenberg, G. Meigs, M. H. Prior, S. Daveau, A. L. Landers, C. L. Cocke, T. Osipov, H. Schmidt-Böcking, and R. Dörner, Phys. Rev. Lett. **92**, 163001 (2004).
[19] W. Vanroose, F. Martin, T. Rescigno, and C. McCurdy, Science **310**, 1787 (2005).
[20] J. Colgan and M. S. Pindzola, J. Phys. B **37**, 1153 (2004).
[21] J. Colgan, M. S. Pindzola, and F. Robicheaux, Phys. Rev. Lett. **98**, 153001 (2007).
[22] J. Colgan, M. Foster, M. S. Pindzola, and F. Robicheaux, J. Phys. B **40**, 4391 (2007).
[23] D. A. Horner, W. Vanroose, T. N. Rescigno, F. Martín, and C. W. McCurdy, Phys. Rev. Lett. **98**, 073001 (2007).
[24] W. Vanroose, D. A. Horner, F. Martín, T. N. Rescigno, and C. W. McCurdy, Phys. Rev. A **74**, 052702 (2006).
[25] T. J. Reddish, J. Colgan, P. Bolognesi, L. Avaldi, M. Gisselbrecht, M. Lavollée, M. S. Pindzola, and A. Huetz, Phys. Rev. Lett. **100**, 193001 (2008).
[26] M. Gisselbrecht, M. Lavollée, A. Huetz, P. Bolognesi, L. Avaldi, D. P. Seccombe, and T. J. Reddish, Phys. Rev. Lett. **96**, 153002 (2006).
[27] H. Sann, T. Jahnke, T. Havermeier, K. Kreidi, C. Stuck, M. Meckel, M. S. Schöffler, N. Neumann, R. Wallauer, S. Voss, A. Czasch, O. Jagutzki, T. Weber, H. Schmidt-Böcking, S. Miyabe, D. J. Haxton, A. E. Orel, T. N. Rescigno, and R. Dörner, Phys. Rev. Lett. **106**, 133001 (2011).
[28] I. Ben-Itzhak, A. Max Sayler, M. Leonard, J. W. Maseberg, D. Hathiramani, E. Wells, M. A. Smith, X. Jiangfan, P. Wang, K. D. Carnes, and B. D. Esry, Nucl. Instrum. Methods Phys. Res. B **233**, 284 (2005).

[29] A. M. Sayler, M. Leonard, K. D. Carnes, R. Cabrera-Trujillo, B. D. Esry, and I. Ben-Itzhak, J. Phys. B **39**, 1701 (2006).
[30] P. J. Richardson, J. H. D. Eland, P. G. Fournier, and D. L. Cooper, J. Chem. Phys. **84**, 3189 (1986).
[31] S. J. King and S. D. Price, Int. J. Mass Spectrom. **277**, 84 (2008).
[32] Z. L. Streeter, F. L. Yip, R. R. Lucchese, B. Gervais, T. N. Rescigno, and C. W. McCurdy, Phys. Rev. A **98**, 053429 (2018).
[33] R. Dörner, V. Mergel, O. Jagutzki, L. Spielberger, J. Ullrich, R. Moshammer, and H. Schmidt-Böcking, Phys. Rep. **330**, 95 (2000).
[34] T. Jahnke, T. Weber, T. Osipov, A. Landers, O. Jagutzki, L. Schmidt, C. Cocke, M. Prior, H. Schmidt-Böcking, R. Dörner *et al.*, J. Electron Spectrosc. Relat. Phenom. **141**, 229 (2004).
[35] J. Ullrich, R. Moshammer, A. Dorn, R. Dörner, L. P. H. Schmidt, and H. Schmidt-Böcking, Rep. Prog. Phys. **66**, 1463 (2003).
[36] O. Jagutzki, A. Cerezo, A. Czasch, R. Dörner, M. Hattas, M. Huang, V. Mergel, U. Spillmann, K. Ullmann-Pfleger, T. Weber, H. Schmidt-Böcking, and G. Smith, IEEE Trans. Nucl. Sci. **49**, 2477 (2002).
[37] B. Gervais, E. Giglio, L. Adoui, A. Cassimi, D. Duflot, and M. E. Galassi J. Chem. Phys. **131**, 024302 (2009).
[38] B. Gaire, I. Bocharova, F. P. Sturm, N. Gehrken, J. Rist, H. Sann, M. Kunitski, J. Williams, M. S. Schöffler, T. Jahnke, B. Berry, M. Zohrabi, M. Keiling, A. Moradmand, A. L. Landers, A. Belkacem, R. Dörner, I. Ben-Itzhak, and T. Weber, Phys. Rev. A **89**, 043423 (2014).
[39] J. H. D. Eland, Chem. Phys. **323**, 391 (2006).
[40] T. Schneider, P. L. Chocian, and J.-M. Rost, Phys. Rev. Lett. **89**, 073002 (2002).
[41] A. Knapp, M. Walter, T. Weber, A. L. Landers, S. Schössler, T. Jahnke, M. Schöffler, J. Nickles, S. Kammer, O. Jagutzki, L. P. H. Schmidt, T. Osipov, J. Rösch, M. H. Prior, H. Schmidt-Böcking, C. L. Cocke, J. Feagin, and R. Dörner, J. Phys. B **35**, L521 (2002).
[42] C. Moore, *CRC Series in Evaluated Data in Atomic Physics* (CRC Press, Boca Raton, FL, 1993), p. 339.
[43] R. Wehlitz, F. Heiser, O. Hemmers, B. Langer, A. Menzel, and U. Becker, Phys. Rev. Lett. **67**, 3764 (1991).
[44] M. Pont and R. Shakeshaft, Phys. Rev. A **54**, 1448 (1996).
[45] A. S. Kheifets and I. Bray, Phys. Rev. A **75**, 042703 (2007).
[46] R. Dörner, J. M. Feagin, C. L. Cocke, H. Bräuning, O. Jagutzki, M. Jung, E. P. Kanter, H. Khemliche, S. Kravis, V. Mergel, M. H. Prior, H. Schmidt-Böcking, L. Spielberger, J. Ullrich, M. Unversagt, and T. Vogt, Phys. Rev. Lett. **77**, 1024 (1996).
[47] A. Ponzi, C. Angeli, R. Cimiraglia, S. Coriani, and P. Decleva, J. Chem. Phys. **140**, 204304 (2014).
[48] P. O'Keeffe, P. Bolognesi, A. Moise, R. Richter, Y. Ovcharenko, and L. Avaldi, J. Chem. Phys. **136**, 104307 (2012).